

## ARTICLE

<https://doi.org/10.1038/s42005-019-0108-x>

OPEN

# Time-resolved electrostatic force microscopy using tip-synchronized charge generation with pulsed laser excitation

Kento Araki<sup>1</sup>, Yutaka Ie<sup>2</sup>, Yoshio Aso<sup>2</sup>, Hiroshi Ohoyama<sup>1</sup> & Takuya Matsumoto<sup>1</sup>

Nanoscale observation of charge distribution and electric polarization is crucial for understanding and controlling functional materials and devices. In particular, the importance of charge dynamics is well recognized, and direct methods to observe charge generation, transfer, and recombination processes are required. Here, we describe tip-synchronized time-resolved electrostatic force microscopy. Numerical modeling clarifies that the tip-synchronized method provides temporal resolution with the timescale of the cantilever oscillation cycle. This method enables us to resolve sub-microsecond charge migration on the surface. The recombination of photo-excited carriers in a bilayer organic photovoltaic thin film is observed as a movie with a 0.3  $\mu\text{s}$  frame step time resolution. Analysis of the images shows that the carrier lifetime is 2.3  $\mu\text{s}$  near the donor/acceptor interface. The tip-synchronized method increases the range of time-resolved electrostatic force microscopy, paving the way for studies of nanoscale charge dynamics.

<sup>1</sup>Department of Chemistry, Graduate School of Science, Osaka University, 1-1 Machikaneyama-cho, Toyonaka, Osaka 560-0043, Japan. <sup>2</sup>The Institute of Scientific and Industrial Research (ISIR), Osaka University, 8-1 Mihogaoka, Ibaraki, Osaka 567-0047, Japan. Correspondence and requests for materials should be addressed to T.M. (email: [matsumoto-t@chem.sci.osaka-u.ac.jp](mailto:matsumoto-t@chem.sci.osaka-u.ac.jp))

Electrostatic force microscopy (EFM) has attracted much attention as a reliable method for visualizing electrostatic information, including charge distribution and polarization state, with molecular-scale spatial resolution<sup>1</sup>. EFM observations are essential for understanding the fundamental characteristics of natural and artificial light-harvesting systems, catalysis, batteries, solar cells, and organic devices<sup>2–7</sup>. In particular, charge transfer and migration dynamics play vital roles in the function of these systems. Therefore, the development of time-resolved EFM (tr-EFM) for studying nanomaterials and nanodevices is required.

Scanning probe microscopy (SPM) is intrinsically a slow method because a high-impedance detection system is essential to achieve high sensitivity and spatial resolution. High-speed scanning tunneling microscopy (STM) and atomic force microscopy (AFM) have provided real-time observations of crystal growth and biological molecular motion<sup>8,9</sup>, but these observations are limited to the millisecond timescale.

The pump-probe method has been used to achieve time resolutions faster than the millisecond timescale. In 1990, Hamers and Cahill reported a time-resolved STM method using the detection of nonlinear tunneling current, and performed a photo-induced carrier relaxation time measurement on Si(111)-(7 × 7)<sup>10</sup>. Recently, Shigekawa et al. reported femtosecond time resolution for GaNAs and other materials<sup>11,12</sup>. A similar approach was also applied to EFM, and a femtosecond force response was reported by Grutter and coworkers<sup>13</sup>. These methods are based on nonlinear charge excitation and relaxation processes, and thus can only be used near saturation. Therefore, the time-resolved detection of charge itself is expected to extend the scope of the technique's applications.

In many instances, microsecond time resolution is enough to observe charge transfer, migration, and recombination because the timescale of charge behavior is much slower than that of energy transfer processes. Even over nanometer distances, a microsecond lifetime is reported for charge migration between surface states on a Si(001) surface<sup>14</sup>. Therefore, sub-microsecond and microsecond timescales are the targets for tr-EFM. Several studies have focused on microsecond tr-EFM. Ginger and coworkers reported sub-microsecond tr-EFM that records the full cantilever deflection signal after light pulse irradiation and analyses the frequency shift using the Hilbert transform to investigate carrier dynamics caused by electric or light pulses<sup>15,16</sup>. Their tr-EFM technique achieves a wide time resolution range from sub-microsecond to millisecond. Collins et al. have also reported time-resolved method called G-mode Kelvin probe force microscopy, which combines the capture of the full cantilever oscillation at the sampling rate limit (~4–10 MHz) and post data processing (filtering and statistical analysis)<sup>17</sup>.

We have proposed a method for achieving microsecond time-resolved force detection using synchronization with the cantilever motion in the previous report<sup>18</sup>. Marohn' group reported a similar time-resolved technique using a synchronization of cantilever oscillation and transient perturbation such as a light or voltage pulse<sup>19</sup>. These methods achieved microsecond time resolution for force detection, but does not visualize charge behavior as images. In this article, the time-resolved imaging of photo-excited charge behavior is demonstrated by tip-synchronized tr-EFM for organic photovoltaics (OPVs).

OPVs are promising next-generation power generation devices. Many approaches for improving the performance of OPVs have been reported, including molecular synthesis, micromorphology control, and design of device structures<sup>20–27</sup>, all of which focus on

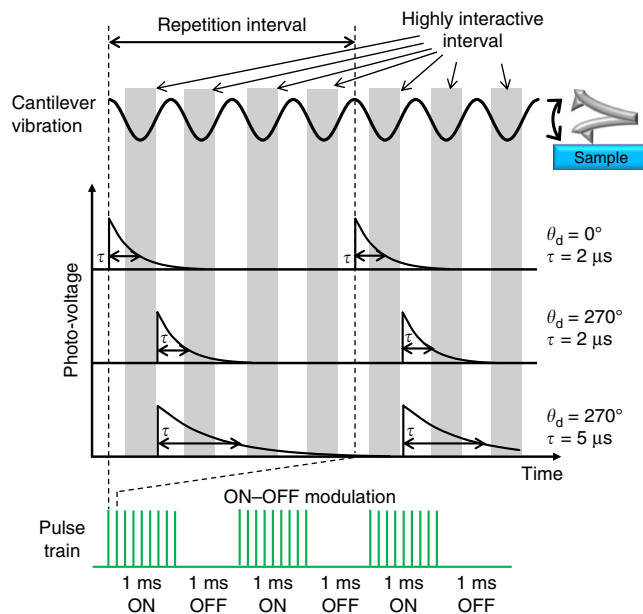


**Fig. 1** Principle of tip-synchronized time-resolved electrostatic force microscopy. Schematic of the synchronization between tip motion and photo-voltage and ON/OFF modulation of pulse train for lock-in detection. The time period when the tip is close to the sample surface is used as a highly interactive interval for detecting the pulsed photo-voltage

controlling the nanoscale charge separation and recombination essential for efficient charge collection.

Here, we describe the principle of tip-synchronized tr-EFM and evaluate its time resolution by numerical modeling. We show that the method is useful for observing charge dynamics, including charge relaxation at the donor–acceptor interface, and present a movie of a recombination process inside an OPV film.

## Results

**Principle of tip-synchronized tr-EFM.** The time response of frequency shift mode EFM is usually limited by the bandwidth of the phase-locked loop (PLL) circuit. To overcome this limitation, we developed tip-synchronized tr-EFM, which is a pump-probe method enabling us to detect microsecond lifetime local charges directly with the repetition rate of the cantilever vibration frequency. This method does not require nonlinear characteristics for charge generation near saturation<sup>18</sup>. The cantilever vibration provides the periodic approach of the tip to the sample surface, and this is the highly interactive interval for transient charge detection (Fig. 1). For large amplitudes, the variation of the tip-sample electrostatic interaction during the oscillation cycle is sufficient for time-resolved observations. Therefore, by adjusting the delay time of the charge excitation against the moment of nearest tip position to the sample surface, the frequency shift could probe time-dependent information about charge dynamics without post signal processing. In our experiment, we irradiated the pulsed light once in four oscillation cycle of cantilever, namely, light pulse irradiation frequency is  $1/4\omega$ , where  $\omega$  is a temporal cantilever oscillation angular frequency. We also used ON/OFF modulation of the pulse train for lock-in detection of a frequency shift (Fig. 1).

Frequency shift,  $\Delta f$ , and amplitude,  $A$ , of the cantilever oscillation for a non-steady-state electrostatic interaction between

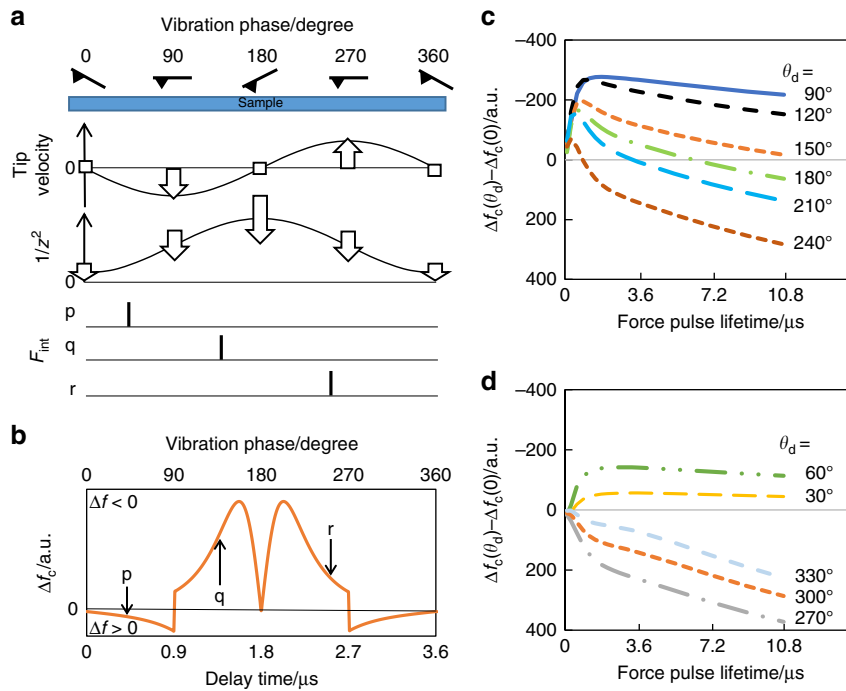


**Fig. 2** Frequency shift behavior in time-resolved electrostatic force microscopy. **a** Timing chart of cantilever position, cantilever velocity, interaction force factor between a tip and a sample surface  $1/z^2$ , and various timing of instantaneous force pulses  $p$ ,  $q$ , and  $r$ . **b** Calculated frequency shift caused by instantaneous force pulse. **c, d** Frequency shift difference as a function of force pulse lifetime under various phase delay  $\theta_d$

the tip and sample surface are expressed as

$$\Delta f \approx -\frac{1}{4\pi^2 mA} \int_0^{2\pi/\omega} F_{\text{int}}(t) \cos \omega t dt \quad (1)$$

$$F_0 A \pi \approx \frac{(1/2)m\omega_0^2 A^2 \cdot 2\pi}{Q} + \omega A \int_0^{2\pi/\omega} F_{\text{int}}(t) \sin \omega t dt \quad (2)$$

where  $m$  is the effective mass of the cantilever,  $F_{\text{int}}(t)$  is the interaction force between the tip and the sample surface,  $\omega$  is the oscillation frequency,  $F_0$  is the excitation force for cantilever vibration, and  $Q$  is the quality factor of a cantilever mechanical resonance.

In the EFM measurements, the tip-sample interaction force,  $F_{\text{int}}(t)$ , can be separated into several kinds of forces  $F_{\text{int}}(t) = F_{\text{vdw}}(t) + F_{\text{ele}}(t) + F_{\text{others}}(t)$ , where  $F_{\text{vdw}}(t)$  is the van der Waals force including the repulsive and attractive regions in short and long tip-sample distances,  $F_{\text{ele}}(t)$  is electrostatic force between the tip and sample, and  $F_{\text{others}}(t)$  consists of various forces, such as the adhesion force and chemical interaction force, and is assumed to be constant in a scanning area.

Generally, frequency modulation SPM is performed in the attractive force region by constant frequency shift feedback under constant oscillation amplitude conditions using an automatic gain control system. The averaged tip-sample distance is kept constant and the  $\Delta f$  value reflects the integral of  $F_{\text{int}}(t) \cos \omega t$  without causing interference with the variation in  $A$ . However, energy dissipation between the tip and sample surface varies widely during scans. Consequently,  $F_{\text{int}}(t)$  involves large variations in  $F_{\text{vdw}}(t)$  depending on the tip position in the scanning area. This problem can be avoided by constant amplitude feedback under constant cantilever excitation energy conditions with self-oscillation. This setup keeps  $F_{\text{vdw}}(t)$  constant and gives conventional topography that is similar to usual

tapping mode measurements, while simultaneously obtaining frequency shift information reflecting mainly attractive forces in the non-contact region.

The electrostatic energy,  $U$ , is determined by capacitance  $C$  and voltage difference  $V$  between the tip and sample. Accordingly, the electrostatic force,  $F_{\text{ele}}$ , is expressed in differential form as

$$F_{\text{ele}} = \frac{\partial U}{\partial z} = \frac{1}{2} \frac{\partial C}{\partial z} V^2 = -\frac{1}{2} \frac{\epsilon S}{z^2} V^2 \quad (3)$$

where  $z$ ,  $\epsilon$ , and  $C$  are the tip-sample distance, the dielectric constant and the capacitance between a tip apex and a sample, respectively. When the pulsed laser irradiates the sample surface and generates transient charges at time  $t_d$ , charge-induced surface voltage  $V_c$  gives a transient change in  $F_{\text{ele}}$  during a cycle of cantilever vibration, resulting in frequency shift variation

$$\Delta f_c(t_d) \approx -\frac{V_0}{4\pi m A^2} \int_{t_d}^{2\pi/\omega} F_{\text{ele}}(t) \cos \omega t dt = -\frac{V_0}{4\pi m A^2} \int_{t_d}^{2\pi/\omega} G(t) \cdot V_c(t) dt + \text{const} \quad (4)$$

where  $V_0$  is the DC bias voltage applied to the sample and  $G(t) = (\epsilon S \cos \omega t) / (z_0 + A \cos \omega t)^2$  is a window function for detecting the time-dependent  $V_c(t)$ . The detailed derivation of Eq. (4) is provided in Methods section.

The electrostatic interaction between the tip and sample is an attractive force, resulting in a negative frequency shift in the attractive potential region. However, the tip-synchronized pulsed force measurements give more complicated behaviors, which is an advantage for the time resolution. Figure 2 shows the variation of  $\Delta f_c$  induced by the pulsed electrostatic force between the tip and sample.  $\Delta f_c$  depends on tip velocity and tip-sample distance when the pulsed surface photo-voltage is generated. Figure 2a shows the timing chart of the relationship between the vibrating tip motion and instantaneous force pulses denoted by  $p$ ,  $q$ , and  $r$ .

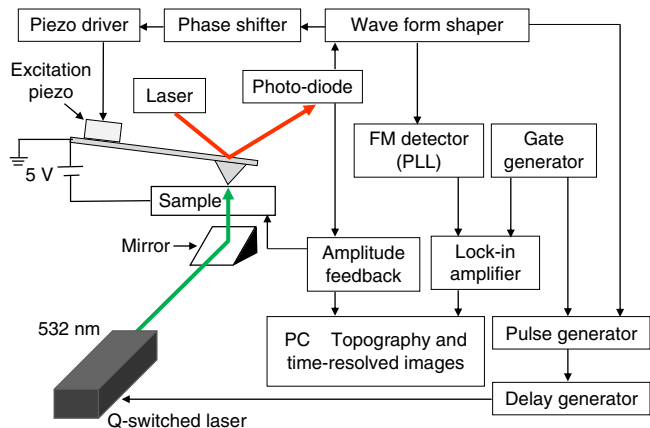


**Fig. 3** Schematic of tip-synchronized electrostatic force microscope setup. The cantilever is operated by self-excitation at its resonant frequency. The deflection of cantilever is detected by a conventional optical lever system. The Q-switched laser is driven using the trigger signal generated by the cantilever deflection signal as a reference oscillator. For this trigger signal, delay control is employed using the delay generator. The deflection signal is demodulated by the phase-locked loop (PLL) to obtain the frequency shift  $\Delta f$  value. The  $\Delta f$  signal is put into a lock-in amplifier to obtain frequency shift variation  $\Delta f_c$  induced by the transient surface charge generation with a reference of the 500 Hz gating signal employing ON/OFF modulation of the laser pulse train. The lock-in amplifier output is used for obtaining  $\Delta f_c$  images, with simultaneous acquisition of topography under constant amplitude feedback conditions

The effect of these impulses on  $\Delta f_c$  is shown in Fig. 2b, where the  $\Delta f_c$  variation caused by the instantaneous force pulse is plotted as a function of delay time (phase delay) from 0 to 3.6  $\mu\text{s}$  that correspond to the phase range from  $0^\circ$  to  $360^\circ$  for a tip vibration of 279 kHz. At  $\theta = 0^\circ$ , the tip is located at the furthest position from the sample surface and the tip velocity is zero. At this moment, the instantaneous force pulse has no effect on  $\Delta f_c$ . When the tip crosses the mid-point of the cantilever vibration at  $\theta = 90^\circ$ , the tip velocity reaches its maximum and the direction of acceleration is inverted. With this inversion, the effect of the pulsed electrostatic force also changes from increasing to reducing the cantilever vibration, corresponding to the apparent spring constant changing from increasing to decreasing;  $\Delta f_c$  changes from positive to negative. As the tip approaches the surface, the electrostatic force rapidly increases.

Figure 2c, d show the behavior of frequency shift for the force pulse with lifetime  $\tau$ . The frequency shift is calculated as a function of force pulse lifetime with various phase delay  $\theta_d$ . Because of the periodic tip motion, it is useful to represent the delay time  $t_d$  as the phase delay of vibration  $\theta_d = \omega t_d$ , where  $\theta_d = 0$  means that the force pulse occurs when the tip is the furthest from the sample surface. To consider the frequency shift behavior,  $\Delta f_c(\theta_d = 0^\circ)$  is used as a reference for  $\Delta f_c(\theta_d)$  with various  $\theta_d$  values. The calculation is performed for four cycles of tip vibration, including the first cycle when force pulse is applied. The assumed force decay curve used here has a fixed rise time of 10 ns and the variable parameters: phase delay ( $\theta_d = 30^\circ$ – $330^\circ$ ) and decay time ( $\tau = 0$ – $6\pi/\omega$ ). When  $\theta_d = 90$ – $240^\circ$ ,  $\Delta f_c$  rapidly increases as the force pulse lifetime increases in the region of  $\tau = 0$ – $1 \mu\text{s}$ . The phase delay is set to  $\theta_d = 270$ – $330^\circ$ ,  $\Delta f_c$  is less sensitive to changes in  $\tau$  value, but we can probe the  $\tau$  value in the range of 0.1 to several tens of microseconds (up to 10.8  $\mu\text{s}$  is shown in Fig. 2c, d). This implies that decay time resolutions of more than two orders of magnitude from sub-microsecond to several tens of microseconds can be achieved with a conventional cantilever (resonant frequency of 300 kHz,  $\omega = 6\pi \times 10^5 \text{ rad/s}$ ).

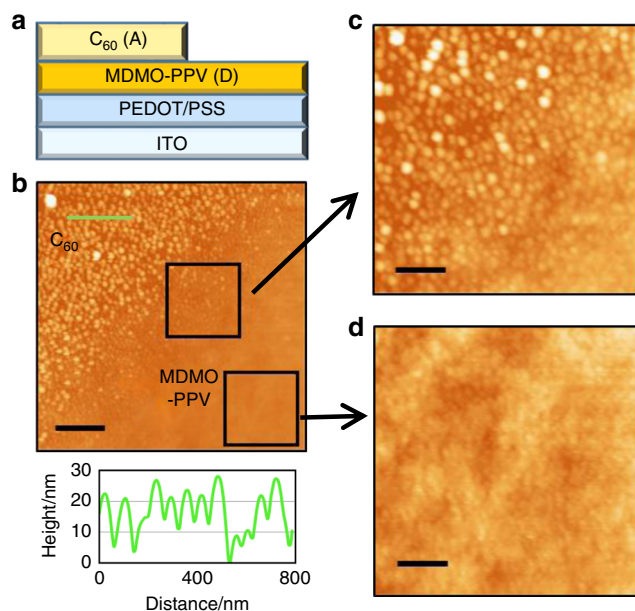


**Fig. 4** Surface morphology of pattern-limited bilayer organic photovoltaic (OPV). **a** Schematic of the pattern-limited bilayer OPV thin film comprised of  $C_{60}$  overlayer and poly[2-methoxy-5-(3',7'-dimethyloctyloxy)-1,4-phenylenevinylene] (MDMO-PPV) on a hole transport layer of poly(3,4-ethylenedioxythiophene)/poly(styrene sulfonate) (PEDOT/PSS). The substrate is indium tin oxide (ITO). **b** Wide-range atomic force microscope image and section profile. The  $C_{60}$  overlayer is visible in the top-left region. The scale bar shows 710 nm. **c, d** Magnified images of an edge region of the  $C_{60}$  overlayer and MDMO-PPV surface in a region away from the  $C_{60}$  layer. The scale bars show 250 nm

**Experimental setup.** A schematic of the tr-EFM system is shown in Fig. 3. The cantilever is operated by self-excitation at its resonant frequency. A DC bias voltage of  $V_0 = -5 \text{ V}$  is applied to the indium tin oxide (ITO) substrate for effective charge collection. The sample is irradiated with pulsed laser light (intensity: 200 mW; wavelength: 532 nm; pulse duration: 10–25 ns; peak power: 100 W) from the back of the substrate without focusing. The beam diameter is approximately 2 mm. The light path and geometry around the sample are represented in Supplementary Figure 1. The deflection of cantilever is detected by a conventional optical lever system. The trigger signal for controlling the laser pulse timing to tip motion is generated by the cantilever deflection signal as a reference oscillator with phase synchronization. Using this trigger signal, delay control is employed for pulsed laser irradiation. This setup maintains the well-defined timing of the pulsed laser irradiation to the fluctuating cantilever oscillation during frequency shift mode operation. The timing chart is shown in Supplementary Figure 2. The deflection signal is demodulated by the PLL to obtain the  $\Delta f$  value.  $\Delta f$  signal is put into a lock-in amplifier to obtain  $\Delta f_c$  with a reference for the 500 Hz ON/OFF modulation of the laser pulse train. The lock-in amplifier output is used for  $\Delta f_c$  image construction, with simultaneous acquisition of topography under constant amplitude feedback conditions.

**Surface morphology.** We fabricated bilayer OPV films consisting of a poly[2-methoxy-5-(3',7'-dimethyloctyloxy)-1,4-phenylenevinylene] (MDMO-PPV) (donor) layer and a pattern-limited (partially deposited)  $C_{60}$  (acceptor) layer. The bilayer films were deposited on a poly(3,4-ethylenedioxythiophene)/poly(styrene sulfonate) (PEDOT/PSS) hole injection layer coated on the ITO substrates. The schematic of the sample is shown in Fig. 4a. The

photovoltaic characteristics used in this study are summarized in Supplementary Figure 3 and Supplementary Table 1.

AFM images in Fig. 4b clearly show that there are many particles in the unmasked area (left upper region) after  $C_{60}$  deposition. These particles are a few tens of nanometers in height, which is much higher than the molecular diameter of  $C_{60}$ . This suggests that  $C_{60}$  molecules diffuse and aggregate on the MDMO-PPV layer. Thus, the edge of the patterned  $C_{60}$  layer is blurred, as shown in Fig. 4c, where the density of  $C_{60}$  particles decreases gradually and the particle size decreases with increasing distance from the boundary. In the region  $>500$  nm from the boundary, there are few  $C_{60}$  particles (Fig. 4d) and the surface morphology is similar to that of the MDMO-PPV single layer (the topography of MDMO-PPV film is provided in Supplementary Figure 4). The AFM observations of the surfaces of the bilayer pattern-limited OPV samples suggest that the samples would be useful for tracking charge dynamics.

**Surface area dependence of frequency shift distribution.** The delay time dependence of  $\Delta f_c$  also has a spatial distribution on the sample surface. The spatial distribution was measured in region A and B of the topography in Fig. 5a. The section profile along line C–D is shown in Fig. 5b. Region A is at the edge of the  $C_{60}$  (acceptor) layer and region B is on the MDMO-PPV (donor) layer far from the edge of the  $C_{60}$  layer. For these areas,  $\Delta f_c$  values are obtained for all pixels in the scanning area and the distributions of  $\Delta f_c$  values are plotted in Fig. 5c (region A) and Fig. 5d (region B) for several delay time settings. The most probable value of each  $\Delta f_c$  distribution is plotted as a function of delay time. In region A,  $\Delta f_c$  has a wide distribution that depends on the delay time. This suggests that the microsecond component of the surface photo-voltage is generated inhomogeneously reflecting the local electronic properties of the surface and interface of the OPV sample. In contrast,  $\Delta f_c$  detected in region B has a narrow distribution with no delay time dependence, indicating that the microsecond component of the surface photo-voltage is averaged out or is not present in region B. This is also an indication that the setup of the apparatus used in this study is effective to obtain microsecond  $\Delta f$  variation selectively and exclude slow response including surface charge accumulation as shown in Supplementary Figures 5 and 6.

**tr-EFM imaging.** Tip-synchronized tr-EFM reflects the spatial distribution and transient changes in  $\Delta f_c$ . This implies that this method can produce a movie-like image sequence of surface potential change. We focus on the edge of the  $C_{60}$  (acceptor) layer on the MDMO-PPV (donor) layer. In Fig. 6a–d, the topography and tr-EFM images obtained for various delay time settings of the pulsed laser irradiation against the vibrating tip motion with  $t_d = 0.0, 0.6$  and  $1.6 \mu\text{s}$ , respectively. The tr-EFM video is available in a Supplementary Movie 1. Here, we choose the starting time of surface potential evolution as  $t_d = 0.0$  when the frequency shift reaches its maximum on the  $C_{60}$  layer (when  $\theta_d = 90^\circ$  in Fig. 2c). This is because we assume that photo-excited charges are generated immediately during the nanosecond light pulse irradiation, and then charge migration and recombination occur on a microsecond timescale. Each tr-EFM image is taken simultaneously with the corresponding topography and these topographies show no difference while several tr-EFM images are acquired (data not shown). The section profiles of the topography and tr-EFM images are shown in Fig. 6e. The height of  $C_{60}$  layer is about 30 nm and the flatness of the  $C_{60}$  and MDMO-PPV films are ca. 0.6 and 1.1 nm, respectively.

There are differences between the topography (Fig. 6a) and tr-EFM images (Fig. 6b–d). In the tr-EFM images, a bright contrast region appears on the  $C_{60}$  layer despite the flat terrace in the topography, whereas the pit indicated by the arrow in the MDMO-PPV terrace does not appear in tr-EFM images. Furthermore, as the delay time increases, the brightness of the  $C_{60}$  layer decreases and a valley near the  $C_{60}$  layer edge appears at  $t_d = 1.6 \mu\text{s}$ , as shown in the tr-EFM images (Fig. 6b–d) and section profiles (Fig. 6e).

## Discussion

The apparent differences between topography and tr-EFM images mentioned above indicate that tip-synchronized tr-EFM detects the charge distribution generated by the photo-excitation at the MDMO-PPV/ $C_{60}$  (donor–acceptor) interface, reflecting the inhomogeneous electronic properties due to the defects in the MDMO-PPV/ $C_{60}$  interface. In particular, the valley is an electrically neutral region where the frequency shift is reduced to zero. This result indicates that the edge of the  $C_{60}$  layer is a carrier recombination site, and that recombination occurs in a few microseconds. Moreover, the MDMO-PPV region also shows a slight increase of the frequency shift over time. We believe that this is related to the accumulation of photo-carrier generated in the MDMO-PPV region. Based on these results, charges arising at the MDMO-PPV/ $C_{60}$  interface and photoelectrons generated from the MDMO-PPV layer are initially collected on the sample surface by the tip-sample electric field, and then the surface electrons recombine with holes that are stabilized near the MDMO-PPV/ $C_{60}$  interface (Fig. 6g).

Tip-synchronized tr-EFM provides complicated  $\Delta f_c$  behavior for the delay time setting (Fig. 2). Consequently, numerical calculation is necessary to obtain the absolute value of the charge lifetime. Figure 6f shows the experimental (solid dots) and calculated (colored lines)  $\Delta f_c$  values as a function of delay time. The comparison between the model calculation (Fig. 2c, d) and experimental results (Fig. 6f) is shown in Supplementary Figure 7. The experimental  $\Delta f_c$  values are obtained from the averaged value on the whole  $C_{60}$  layer region for each tr-EFM image. The calculations are performed using Eq. (4) assuming that the photo-voltage arises in 10 ns and decays exponentially with various lifetimes. Comparing the experimental data with simulation results, the overall line shape is reproduced qualitatively and the carrier lifetime of  $2.3 \mu\text{s}$  matches the experimental result well. This  $2.3 \mu\text{s}$  value is reasonable because it is reported that practical organic solar cells using similar materials (bulk heterojunction solar cell made of a *p*-phenylene vinylene/ $C_{60}$  system) have carrier lifetimes of  $2.5\text{--}40 \mu\text{s}$ <sup>28</sup>.

In summary, we have developed tr-EFM using tip-synchronized charge generation. We obtained movie-like images showing the charge dynamics for a bilayer OPV sample. We also determined the carrier lifetime of  $2.3 \mu\text{s}$  by comparing the experimental data with the simulation results. This method is suitable for studying a variety of charge dynamics occurring in processes such as artificial photosynthesis and photocatalysis and to improve our understanding of molecular and organic devices.

## Methods

**Numerical modeling.** Electrostatic force between the tip apex and sample surface ( $F_{\text{ele}}$ ) is given by

$$F_{\text{ele}} = -\frac{1}{2z^2} V^2 = \frac{1}{2z^2} (V_0 + V_c(t))^2 = \frac{1}{2z^2} (V_0^2 + 2V_0 V_c(t) + V_c(t)^2),$$

where  $V_0$  is a DC bias voltage applied to the sample and  $V_c(t)$  is the photo-induced voltage. In the usual condition of  $V_c(t) \ll V_0$ , the expression of  $F_{\text{ele}}$  can be simplified to

$$F_{\text{ele}} = -\frac{1}{2z^2} (V_0^2 + 2V_0 V_c(t)).$$

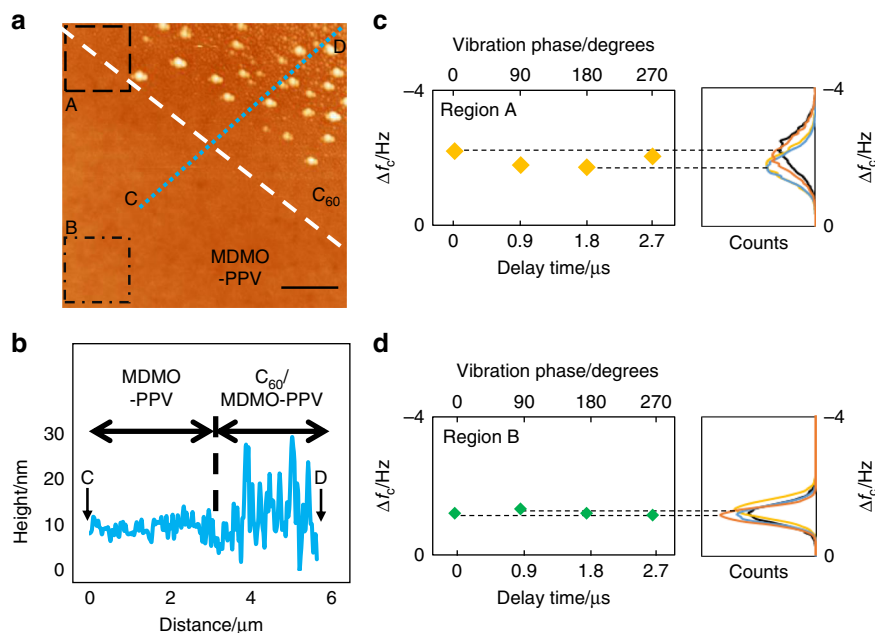


**Fig. 5** Frequency shift distribution induced by pulsed photo-voltage generation. **a** Topography of pattern-limited bilayer organic photovoltaic film surface. The C<sub>60</sub> layer is deposited in the top-right region, indicated by a broken line. The scale bar shows 1.2 μm. **b** A section profile on the dotted C-D line in Fig. 5a. **c, d** Frequency shift distributions and their peak values obtained in region A (near the C<sub>60</sub> layer) (**c**) and in region B (far from the C<sub>60</sub> layer) (**d**). The typical error of the frequency shift measurement is less than 0.1 Hz. In region A, the frequency shift shows a broader distribution than that in region B. The distributions are arisen from the inhomogeneous surface charges. The peak variation of the distribution depending on the photo-irradiation delay time occurs only in region A

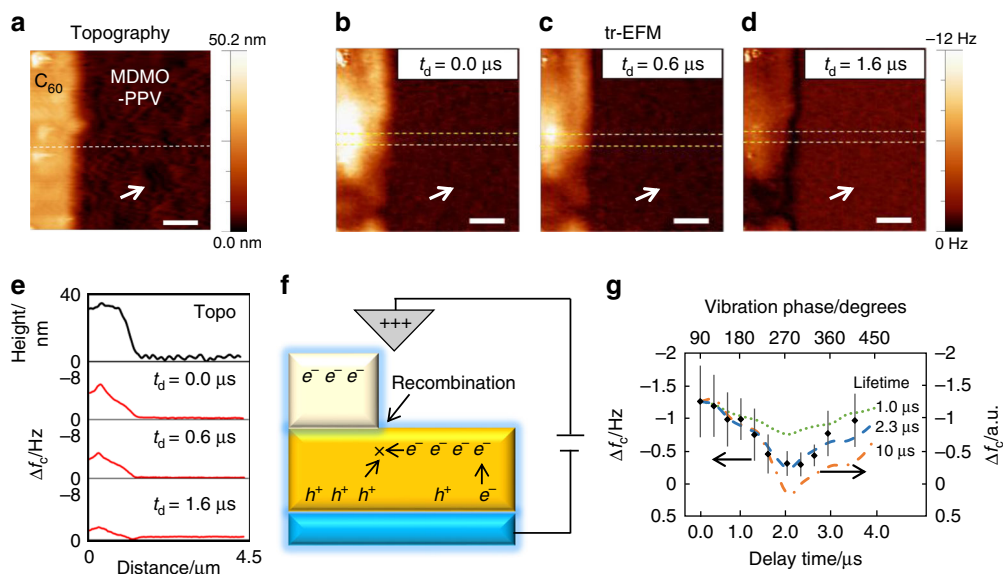


**Fig. 6** Frame step time-resolved electrostatic force observation. **a** Topography of the edge of C<sub>60</sub> (acceptor) overlayer on the poly[2-methoxy-5-(3',7'-dimethyloctyloxy)-1,4-phenylenevinylene] (MDMO-PPV, donor) layer. The scale bar shows 900 nm. **b-d** Time-resolved electrostatic force microscope (tr-EFM) images observed at delay time  $t_d = 0.0, 0.6,$  and  $1.6 \mu\text{s}$  for the corresponding area of the topography. Topography and tr-EFM images are obtained simultaneously and all the images for different  $t_d$  are taken of the same area. The arrows indicate the position where a pit exists in the topography. **e** Section profiles of the topography and each tr-EFM image. The section profile of topography is taken on a broken line in **a**. Section profiles of tr-EFM images show the average inside the two broken lines in **b-d**. **f** Schematic representation of charge transfer and recombination processes. Top, middle, and bottom layers correspond to C<sub>60</sub>, MDMO-PPV, and the electrode, respectively. **g** Comparison of the experimental values (black dots) measured on the C<sub>60</sub> layer and calculated (colored lines) frequency shifts depending on delay time. The bars for experimental results show the standard deviation of frequency shift distribution. This distribution is arisen from inhomogeneous surface charges induced by light excitation. The lines indicate the calculation results with 1.0, 2.3, and 10 μs lifetimes. The calculation with 2.3 μs carrier lifetime fits the experimental results well

From Eq. (1), the electrostatic component of frequency shift ( $\Delta f_{\text{ele}}$ ) can be divided into components as

$$\begin{aligned} \Delta f_{\text{ele}} &\propto \int_0^{2\pi/\omega} F_{\text{ele}} \cos \omega t \, dt = \\ &-\frac{1}{2} \varepsilon S V_0^2 \int_0^{2\pi/\omega} \frac{\cos \omega t}{(z_0 + A \cos \omega t)^2} \, dt \\ &-\varepsilon S V_0 \int_0^{t_d} \frac{\cos \omega t}{(z_0 + A \cos \omega t)^2} V_c(t) \, dt \\ &-\varepsilon S V_0 \int_{t_d}^{2\pi/\omega} \frac{\cos \omega t}{(z_0 + A \cos \omega t)^2} V_c(t) \, dt, \end{aligned}$$

where  $t_d$  is a delay time. Because the first part is constant and  $V_c(t) = 0$  when  $t < t_d$ , a frequency shift is caused by pulsed photo-irradiation with the timing  $t_d$ :

$$\Delta f_c(t_d) \propto -\varepsilon S V_0 \int_{t_d}^{2\pi/\omega} \frac{\cos \omega t}{(z_0 + A \cos \omega t)^2} V_c(t) \, dt.$$

By comparison with Eq. (1) in the main text,  $\Delta f_c(t_d)$  can be expressed in the following form:

$$\Delta f_c(t_d) = \frac{V_0}{4\pi^2 m A} \int_{t_d}^{2\pi/\omega} G(t) V_c(t) \, dt,$$

where  $G(t) = \varepsilon S \cos \omega t / (z_0 + A \cos \omega t)^2$  is a window function.

**Sample preparation.** MDMO-PPV and  $C_{60}$  were purchased from Sigma-Aldrich and used without further purification. The ITO substrates are provided from Techno Print. The ITO substrate was ultrasonically cleaned and hydrophilized by UV-ozone treatment. The PEDOT/PSS layer was prepared on the ITO substrate by spin-casting, and was annealed at 135 °C for 10 min under ambient conditions. A 0.12 wt% MDMO-PPV toluene solution was stirred for 2 h at room temperature under a nitrogen atmosphere. The MDMO-PPV layer was deposited onto the PEDOT/PSS layer by spin-casting and was annealed at 145 °C for 15 min under a nitrogen atmosphere. A silicon plate was applied to the MDMO-PPV film as a mask, and  $C_{60}$  was deposited by thermal vapor deposition.

**tr-EFM measurements.** All measurements were performed with a SPM (JSPM4200, JEOL) under vacuum conditions ( $10^{-3}$  Pa) at room temperature. Rectangular Pt/Ir-coated silicon cantilever probes were used as force sensors (PPP-NCHPt, Nanosensors). The cantilever deflection signal was demodulated using a PLL circuit (OC4 station, Nanonis) and the  $\Delta f_c$  value was detected by a lock-in amplifier (LI5640, NF Corporation). The sample was irradiated with a Q-switched pulse laser (QL-532-200, CrystaLaser; Nd:YAG/Nd:YVO<sub>4</sub>, average power: 200 mW). Pulse irradiation timing was controlled with a delay generator (DG645, Stanford Research), and the pulse train was modulated by the 500 Hz of ON/OFF switching using a function generator (SG-4105, Iwatsu).

## Data availability

The data that support the findings of this study are available from the corresponding author upon reasonable request.

Received: 19 June 2018 Accepted: 24 December 2018

Published online: 25 January 2019

## References

- Schuler, B. et al. Contrast formation in Kelvin probe force microscopy of single  $\pi$ -conjugated molecules. *Nano Lett.* **14**, 3342–3346 (2014).
- Sasahara, A., Pang, C. L. & Onishi, H. Local work function of Pt clusters vacuum-deposited on a TiO<sub>2</sub> surface. *J. Phys. Chem. B* **110**, 17584–17588 (2006).
- Tait, S. L., Ngo, L. T., Yu, Q., Fain, S. C. & Campbell, C. T. Growth and sintering of Pd clusters on  $\alpha$ -Al<sub>2</sub>O<sub>3</sub>. *J. Chem. Phys.* **122**, 064712 (2005).
- Araki, K., Ie, Y., Aso, Y. & Matsumoto, T. Fine structures of organic photovoltaic thin films probed by frequency-shift electrostatic force microscopy. *Jpn. J. Appl. Phys.* **55**, 070305 (2016).
- Hoppe, H., Sariciftci, N. S. & Hoppe, H. Morphology of polymer/fullerene bulk heterojunction solar cells. *J. Mater. Chem.* **16**, 45–61 (2006).
- Maturová, K. et al. Scanning Kelvin probe microscopy on bulk heterojunction polymer blends. *Adv. Funct. Mater.* **19**, 1379–1386 (2009).
- Zhu, J., Zeng, K. & Lu, L. In-situ nanoscale mapping of surface potential in all-solid-state thin film Li-ion battery using Kelvin probe force microscopy. *J. Appl. Phys.* **111**, 063723 (2012).
- Miyata, K. et al. Dissolution processes at step edges of calcite in water investigated by high-speed frequency modulation atomic force microscopy and simulation. *Nano Lett.* **17**, 4083–4089 (2017).
- Ando, T., Uchihashi, T. & Scheuring, S. Filming biomolecular processes by high-speed atomic force microscopy. *Chem. Rev.* **114**, 3120–3188 (2014).
- Hamers, R. J. & Cahill, D. G. Ultrafast time resolution in scanned probe microscopies. *Appl. Phys. Lett.* **57**, 2031–2033 (1990).
- Terada, Y. et al. Ultrafast photoinduced carrier dynamics in GaNAs probed using femtosecond time-resolved scanning tunnelling microscopy. *Nanotechnology* **18**, 044028 (2007).
- Terada, Y., Yoshida, S., Takeuchi, O. & Shigekawa, H. Real-space imaging of transient carrier dynamics by nanoscale pump-probe microscopy. *Nat. Photonics* **4**, 869–874 (2010).
- Schumacher, Z., Spielhofer, A., Miyahara, Y. & Grutter, P. The lower limit for time resolution in frequency modulation atomic force microscopy. *Appl. Phys. Lett.* **110**, 053111 (2017).
- Jung, W., Cho, D., Kim, M.-K., Choi, H. J. & Lyo, I.-W. Time-resolved energy transduction in a quantum capacitor. *Proc. Natl Acad. Sci.* **108**, 13973–13977 (2011).
- Giridharagopal, R. et al. Submicrosecond time resolution atomic force microscopy for probing nanoscale dynamics. *Nano Lett.* **12**, 893–898 (2012).
- Karatay, D. U. et al. Fast time-resolved electrostatic force microscopy: achieving sub-cycle time resolution. *Rev. Sci. Instrum.* **87**, 053702 (2016).
- Collins, L. et al. Breaking the time barrier in Kelvin probe force microscopy: fast free force reconstruction using the G-mode platform. *ACS nano* **11**, 8717–29 (2017).
- Matsumoto, T. & Kawai, T. Time-resolved electrostatic force detection using scanning probe microscope. *Microscopy* **43**, 149–151 (2008).
- Dwyer, R. P., Nathan, S. R. & Marohn, J. A. Microsecond photocapacitance transients observed using a charged microcantilever as a gated mechanical integrator. *Sci. Adv.* **3**, 1–14 (2017).
- Brabec, B. C. J., Sariciftci, N. S. & Hummelen, J. C. Plastic solar cells \*\*. *Adv. Funct. Mater.* **11**, 15–26 (2001).
- Blom, B. P. W. M., Mihailetschi, V. D., Koster, L. J. A. & Markov, D. E. Device physics of polymer: fullerene bulk heterojunction solar cells \*\*. *Adv. Mater.* **19**, 1551–1566 (2007).
- Bredas, J.-L., Norton, J. E., Cornil, J. & Coropceanu, V. Molecular understanding of organic solar cells: the challenges. *Acc. Chem. Res.* **42**, 1691–1699 (2009).
- Jinnai, S. et al. Three-dimensional  $\pi$ -conjugated compounds as non-fullerene acceptors in organic photovoltaics: the influence of acceptor unit orientation at phase interfaces on photocurrent generation efficiency. *J. Mater. Chem. A* **5**, 3932–3938 (2017).
- Chen, W., Nikiforov, P. & Darling, S. B. Environmental science morphology characterization in organic and hybrid solar cells. *Energy Environ. Sci.* **5**, 8045–8074 (2012).
- Cheyns, D. et al. Nanoimprinted semiconducting polymer films with 50 nm features and their application to organic heterojunction solar cells. *Nanotechnology* **19**, 424016 (2008).
- Kim, M.-S. et al. Flexible conjugated polymer photovoltaic cells with controlled heterojunctions fabricated using nanoimprint lithography Flexible conjugated polymer photovoltaic cells with controlled heterojunctions fabricated using nanoimprint lithography. *Appl. Physics Lett.* **90**, 123113 (2007).
- Yang, Y., Mielczarek, K., Aryal, M., Zakhidov, A. & Hu, W. Nanoimprinted polymer solar cell. *ACS Nano* **6**, 2877–2892 (2012).
- Mihailetschi, B. V. D. et al. Compositional dependence of the performance of poly(p-phenylene vinylene): methanofullerene bulk-heterojunction solar cells \*\*. *Adv. Funct. Mater.* **15**, 795–801 (2005).

## Acknowledgements

This work is supported by JSPS KAKENHI grant numbers 25110014, 25600099, JP25110004, 16K13667, 18H01872, and by ISIR Nanotechnology Initiative-8475-2016.

## Author contributions

K.A. performed all experiments and numerical modeling described in this manuscript as the Ph.D. work. Y.I. and Y.A. contributed to the OPVs fabrication. H.O. organized the contribution to the numerical modeling. T.M. provided basic idea and supervised the project.

**Additional information**

**Supplementary information** accompanies this paper at <https://doi.org/10.1038/s42005-019-0108-x>.

**Competing interests:** The authors declare no competing interests.

**Reprints and permission** information is available online at <http://npg.nature.com/reprintsandpermissions/>

**Publisher's note:** Springer Nature remains neutral with regard to jurisdictional claims in published maps and institutional affiliations.



**Open Access** This article is licensed under a Creative Commons Attribution 4.0 International License, which permits use, sharing, adaptation, distribution and reproduction in any medium or format, as long as you give appropriate credit to the original author(s) and the source, provide a link to the Creative Commons license, and indicate if changes were made. The images or other third party material in this article are included in the article's Creative Commons license, unless indicated otherwise in a credit line to the material. If material is not included in the article's Creative Commons license and your intended use is not permitted by statutory regulation or exceeds the permitted use, you will need to obtain permission directly from the copyright holder. To view a copy of this license, visit <http://creativecommons.org/licenses/by/4.0/>.

© The Author(s) 2019